The Method of Regularized Stokeslets in Three Dimensions: Analysis, Validation, and Application to Helical Swimming

Ricardo Cortez
Department of Mathematics
Tulane University
6823 St. Charles Ave.
New Orleans, LA, 70118
cortez@math.tulane.edu

Lisa Fauci
Department of Mathematics
Tulane University
6823 St. Charles Ave.
New Orleans, LA, 70118
ljf@math.tulane.edu

Alexei Medovikov
Department of Mathematics
Tulane University
6823 St. Charles Ave.
New Orleans, LA, 70118
amedovik@math.tulane.edu.

February 18, 2004

Abstract

The method of regularized Stokeslets is a Lagrangian method for computing Stokes flow driven by forces distributed at material points in a fluid. It is based on the superposition of exact solutions of the Stokes equations when forces are given by a cutoff function. We present this method in three dimensions, along with an analysis of its accuracy and performance on the model problems of flow past a sphere and the steady state rotation of rigid helical tubes. Predicted swimming speeds for various helical geometries are compared with experimental data for motile spirochetes. In addition, the regularized Stokeslet method is readily implemented in conjunction with an immersed boundary representation of an elastic helix that incorporates passive elastic properties as well as mechanisms of internal force generation.

1 Introduction

There has been enormous success in the study of low Reynolds number fluid dynamics by representing solutions of the Stokes equations as a superposition of fundamental solutions, known as Stokeslets, due to the linearity of the equations. The formulation of the boundary element method for Stokes flow is based on the numerical evaluation of distributions of Stokeslets (the velocity field induced by a point force in an unbounded region) along surfaces [1]. Slender body theories use distributions of Stokeslets and other elements along the centerline of a thin tube to approximate the velocity field due to the motion of the tube in the fluid [2, 3, 4].

The *method of regularized Stokeslets*, originally introduced by Cortez [5], is based on the computation of the velocity field due to a distribution of modified expressions for the Stokeslet in which the singularity has been removed. The regularized expression is derived as the exact solution to the Stokes equations consistent with forces given by regularized delta functions. In this Lagrangian method, trajectories of fluid particles are tracked throughout the simulation. The method is particularly useful when the particles are placed along a surface that deforms due to time-dependent, force-driven fluid motion. Since the Stokes equations are linear, direct summation may be used to compute the velocity at each of the immersed boundary points in order to advance a time step. This method is related to boundary integral methods [1] when the forces lie on the surface of a smooth connected set. However, the method of regularized Stokeslets can also be used in cases where the forces are applied at a discrete collection of points that do not necessarily approximate a smooth interface.

One application that motivates this work is the development of models for the fluid dynamics of motile spirochetes [6] based upon an *immersed boundary framework* [7]. Since viscous forces are

much larger than inertial forces in the realm of microorganism motility, one may use the Stokes equations to describe the fluid dynamics. The force-generating organism is accounted for by suitable contributions to a force density term in the fluid dynamics equations. The force of an organism on the fluid is a delta-function layer of force supported only by the region of fluid that coincides with material points along the surface of the organism; away from these points, this force is zero. The methodology developed here will ultimately allow the coupling of the force-generating mechanisms of a spirochete's internal flagella with its passive elastic structures and the surrounding viscous fluid.

The goal of this paper is two-fold. Firstly, we present the regularized Stokeslet method in three dimensions, along with an analysis of its accuracy and performance for two test problems. Secondly, we present initial results related to the swimming of helical bacteria in three dimensions. There is no restriction placed upon the amplitude or wavelength of the helix, and the thickness of the helix is a parameter that can be varied. We examine both the steady longitudinal progression of a rigid helix that rotates as a result of an externally imposed torque, and the swimming dynamics of an elastic helical body whose rotation is driven by simple, internal motors.

2 Stokes flow driven by regularized forces

In the next two sections, we present the method of regularized Stokeslet based on exact solutions of the Stokes equations for body forces represented by smooth localized elements satisfying the incompressible flow Stokes equations

$$\mu\nabla^2\boldsymbol{u} - \nabla p = -\boldsymbol{g}\phi_\epsilon(\boldsymbol{x} - \boldsymbol{x}_0) \tag{1a}$$

$$\nabla \cdot \boldsymbol{u} = 0 \tag{1b}$$

where $\phi_\epsilon(\boldsymbol{x})$ is a *cutoff function* with the property that $\int \phi_\epsilon(\boldsymbol{x})d\boldsymbol{x} = 1$. We think of $\phi_\epsilon(\boldsymbol{x})$ as a radially symmetric, smooth approximation to a $3D$ delta distribution, so that $\phi_\epsilon(\boldsymbol{x})$ is concentrated near $\boldsymbol{x} = 0$ and ϵ is a small parameter that controls the spreading. Due to the linearity of the equations, the solution for multiple forces of the same form can be obtained by superposition. Regularization techniques that use this type of cutoff function have been used extensively in other Lagrangian methods in fluid dynamics [8, 9] and convection-diffusion [10] processes.

One of the goals in this section is to develop a boundary-integral representation of Stokes flow with the use of regularized forces, since the flow generated by these is given by an integral with nonsingular kernel. One advantage of this formulation is that it leads to stable numerical computations since there is no need to evaluate nearly-singular integrals of the type that arise in the presence of a singular (but integrable) kernel. However, since the cutoff function approaches a delta distribution as $\epsilon \to 0$, the theory developed here includes the traditional formulation in that limit. Another advantage is that the solutions are well defined everywhere even when the forces are not applied on a closed surface but along curves or even discrete points. Those cases cannot be approached with the traditional boundary-integral formulation, since they lead to singular nonintegrable kernels. In these cases, the regularization parameter plays the role of a physical parameter that merely gives the extent of the region where the force is applied since the limit as $\epsilon \to 0$ of the resulting velocity does not exist.

We introduce the regularized Green's function for the velocity $S^\epsilon(\boldsymbol{x}, \boldsymbol{x}_0)$ and write the solution of Eq. (1a)-(1b) in the form

$$u_i(\boldsymbol{x}) = \frac{1}{8\pi\mu} S^\epsilon_{ij}(\boldsymbol{x}, \boldsymbol{x}_0) g_j. \tag{2}$$

(Here, and throughout this manuscript, we use the Einstein summation convention.) This expres-

sion S_{ij}^{ϵ} is also known as a *regularized Stokeslet*. Similarly, we write the pressure and stress tensor associated with the flow as

$$p(\boldsymbol{x}) = \frac{1}{8\pi} P_j^{\epsilon}(\boldsymbol{x}, \boldsymbol{x}_0) g_j \tag{3}$$

$$\sigma_{ik}(\boldsymbol{x}) = \frac{1}{8\pi} T_{ijk}^{\epsilon}(\boldsymbol{x}, \boldsymbol{x}_0) g_j. \tag{4}$$

We note that the Stokes equation (1a), implies that the regularized velocity Green's function must satisfy

$$\nabla^2 S_{kj}^{\epsilon}(\boldsymbol{x}, \boldsymbol{x}_0) - \frac{\partial P_j^{\epsilon}(\boldsymbol{x}, \boldsymbol{x}_0)}{\partial x_k} = -8\pi \delta_{kj} \phi_{\epsilon}(\boldsymbol{x} - \boldsymbol{x}_0) \tag{5a}$$

for any j and k and where δ_{kj} is the Kronecker delta. Similarly, from the incompressibility condition, (1b) we conclude that

$$\frac{\partial S_{ij}^{\epsilon}}{\partial x_i} = 0 \tag{5b}$$

for any j. The last two equations are equivalent to the Stokes equations written for the Green's functions.

We take the derivative of Eq. (5a) with respect to x_k, sum over k, and use Eq. (5b) to get the relation

$$\nabla^2 P^{\epsilon}(\boldsymbol{x}, \boldsymbol{x}_0) = 8\pi \nabla \phi_{\epsilon}(\boldsymbol{x} - \boldsymbol{x}_0).$$

It is convenient to introduce the functions G^{ϵ} and B^{ϵ} as the free-space solutions of the equations

$$\nabla^2 G^{\epsilon}(\boldsymbol{x}) = \phi_{\epsilon}(\boldsymbol{x}), \qquad \nabla^2 B^{\epsilon}(\boldsymbol{x}) = G^{\epsilon}(\boldsymbol{x}),$$

which depend only on the specific form of the cutoff function ϕ_{ϵ}. These functions allow us to express the pressure as

$$P_j^{\epsilon}(\boldsymbol{x}, \boldsymbol{x}_0) = 8\pi \frac{\partial G^{\epsilon}(\boldsymbol{x} - \boldsymbol{x}_0)}{\partial x_j}. \tag{6}$$

Using Eq. (5a), we find that the regularized Green's function for Stokes flow is

$$S_{kj}^{\epsilon}(\boldsymbol{x},\boldsymbol{x}_0) = 8\pi\left[\frac{\partial^2 B^{\epsilon}(\boldsymbol{x}-\boldsymbol{x}_0)}{\partial x_k \partial x_j} - \delta_{kj} G^{\epsilon}(\boldsymbol{x}-\boldsymbol{x}_0)\right]. \tag{7}$$

This expression satisfies exactly the incompressibility condition in Eq. (5b). Since the stress tensor σ is defined as

$$\sigma_{ik}(\boldsymbol{x}) = -\delta_{ik} p(\boldsymbol{x}) + \mu\left(\frac{\partial u_i}{\partial x_k} + \frac{\partial u_k}{\partial x_i}\right),$$

we find that

$$T_{ijk}^{\epsilon}(\boldsymbol{x},\boldsymbol{x}_0) = -\delta_{ik} P_j^{\epsilon}(\boldsymbol{x},\boldsymbol{x}_0) + \mu\left(\frac{\partial S_{ij}^{\epsilon}(\boldsymbol{x},\boldsymbol{x}_0)}{\partial x_k} + \frac{\partial S_{kj}^{\epsilon}(\boldsymbol{x},\boldsymbol{x}_0)}{\partial x_i}\right). \tag{8}$$

For a given radially-symmetric cutoff function ϕ_ϵ, the auxiliary functions G^ϵ and B^ϵ are derived first, and the solution is found from Eq. (6)-(8).

A A specific choice of cutoff ϕ_ϵ

In our computations, we use the cutoff function

$$\phi_\epsilon(\boldsymbol{x}-\boldsymbol{x}_0) = \frac{15\epsilon^4}{8\pi(r^2+\epsilon^2)^{7/2}}, \tag{9}$$

where $r = \|\boldsymbol{x}-\boldsymbol{x}_0\|$. The exponent in the denominator controls the decay of the function as $|\boldsymbol{x}| \to \infty$. In Section 3 we show that the regularization error in the numerical approximation is $O(\epsilon^2)$ if the cutoff function has finite second moment. This requires the denominator to behave asymptotically as r^m with $m > 5$. We choose the function above for convenience in analytically

calculating various moments of ϕ_ϵ. With this choice, one can establish

$$P_j^\epsilon(\boldsymbol{x},\boldsymbol{x}_0) = (x_j - x_{0,j})\frac{2r^2+5\epsilon^2}{(r^2+\epsilon^2)^{5/2}}, \tag{10a}$$

$$S_{ij}^\epsilon(\boldsymbol{x},\boldsymbol{x}_0) = \delta_{ij}\frac{r^2+2\epsilon^2}{(r^2+\epsilon^2)^{3/2}} + \frac{(x_i - x_{0,i})(x_j - x_{0,j})}{(r^2+\epsilon^2)^{3/2}}, \tag{10b}$$

$$\begin{aligned} T_{ijk}^\epsilon(\boldsymbol{x},\boldsymbol{x}_0) &= \frac{-6(x_i - x_{0,i})(x_j - x_{0,j})(x_k - x_{0,k})}{(r^2+\epsilon^2)^{5/2}} \\ &- \frac{3\epsilon^2\big((x_i - x_{0,i})\delta_{jk} + (x_j - x_{0,j})\delta_{ik} + (x_k - x_{0,k})\delta_{ij}\big)}{(r^2+\epsilon^2)^{5/2}}. \end{aligned} \tag{10c}$$

These expressions are regularized versions of the well-known fundamental solution of the Stokes equations. The regularization modifies the fundamental (singular) solution particularly in the near field, $r < O(\epsilon)$, while in the far field $\epsilon \ll r$ the modification is negligible. In the limit as $\epsilon \to 0$, the cutoff function approaches a delta distribution, and the above expressions tend to the singular solution of the Stokes equations. This is, in fact, the case, as one can verify that for $r \neq 0$,

$$\begin{aligned} \lim_{\epsilon\to 0} P_j^\epsilon(\boldsymbol{x},\boldsymbol{x}_0) &= P_j^0(\boldsymbol{x},\boldsymbol{x}_0) \equiv 2\frac{(x_j - x_{0,j})}{r^3}, \\ \lim_{\epsilon\to 0} S_{ij}^\epsilon(\boldsymbol{x},\boldsymbol{x}_0) &= S_{ij}^0(\boldsymbol{x},\boldsymbol{x}_0) \equiv \frac{\delta_{ij}}{r} + \frac{(x_i - x_{0,i})(x_j - x_{0,j})}{r^3}, \\ \lim_{\epsilon\to 0} T_{ijk}^\epsilon(\boldsymbol{x},\boldsymbol{x}_0) &= T_{ijk}^0(\boldsymbol{x},\boldsymbol{x}_0) \equiv \frac{-6(x_i - x_{0,i})(x_j - x_{0,j})(x_k - x_{0,k})}{r^5}, \end{aligned}$$

where S_{ij}^0 is known as a *Stokeslet*.

B The boundary integral equations

It is well known that Stokes flow in smooth bounded sets may be represented in terms of boundary integrals involving the boundary values of the velocity and the surface force (see [11]). This representation is often derived from the Lorentz reciprocal identity relating two solutions of Stokes equations, and identifying one of them with the flow generated by a point force of strength $\boldsymbol{g}$ located

at $\boldsymbol{x}_0$. Here we present a modified version of the reciprocal identity, where one solution is identified with the flow due to a regularized force.

Let D be a solid body and assume that $\boldsymbol{x}$ is outside D. Let $(\boldsymbol{u}, p)$ satisfy

$$\mu\nabla^2\boldsymbol{u} - \nabla p = 0, \qquad \nabla\cdot\boldsymbol{u} = 0,$$

and define the associated stress tensor by

$$\sigma_{ik} = -p\delta_{ik} + \mu\left(\frac{\partial u_i}{\partial x_k} + \frac{\partial u_k}{\partial x_i}\right).$$

Let $(\boldsymbol{u}^\epsilon, p^\epsilon)$ be the solution of the Stokes equation with a regularized force of strength $\boldsymbol{g}$ centered at $\boldsymbol{x}_0$,

$$\mu\nabla^2\boldsymbol{u}^\epsilon - \nabla p^\epsilon = -\boldsymbol{g}\phi_\epsilon(\boldsymbol{x}-\boldsymbol{x}_0), \qquad \nabla\cdot\boldsymbol{u}^\epsilon = 0,$$

and define the associated stress tensor by

$$\sigma^\epsilon_{ik} = -p^\epsilon\delta_{ik} + \mu\left(\frac{\partial u^\epsilon_i}{\partial x_k} + \frac{\partial u^\epsilon_k}{\partial x_i}\right).$$

Since $\partial\sigma_{ik}(\boldsymbol{x})/\partial x_k = 0$ and $\partial\sigma^\epsilon_{ik}(\boldsymbol{x})/\partial x_k = -g_i\phi_\epsilon(\boldsymbol{x}-\boldsymbol{x}_0)$, we find that

$$\frac{\partial}{\partial x_k}\left(u^\epsilon_i\sigma_{ik} - u_i\sigma^\epsilon_{ik}\right) = u_j g_j\phi_\epsilon(\boldsymbol{x}-\boldsymbol{x}_0).$$

We can now substitute the expressions

$$u^\epsilon_i(\boldsymbol{x}) = \frac{1}{8\pi\mu}S^\epsilon_{ij}(\boldsymbol{x},\boldsymbol{x}_0)g_j, \quad \sigma^\epsilon_{ik}(\boldsymbol{x}) = \frac{1}{8\pi}T^\epsilon_{ijk}(\boldsymbol{x},\boldsymbol{x}_0)g_j$$

and note that the coefficients g_j are arbitrary to find that $\boldsymbol{u}$ and σ must satisfy the following reciprocal relation for any j

$$\frac{1}{8\pi\mu}\frac{\partial}{\partial x_k}\left(S^\epsilon_{ij}\sigma_{ik} - \mu u_i T^\epsilon_{ijk}\right) = u_j\phi_\epsilon(\boldsymbol{x}-\boldsymbol{x}_0). \tag{11}$$

This is our version of the Lorentz reciprocal identity.

We now let Ω be the exterior of the solid body D inside a large ball containing D (refer to Figure 1), and we integrate the above expression over Ω to get

$$\frac{1}{8\pi\mu}\int_\Omega \frac{\partial}{\partial x_k}\left(S^\epsilon_{ij}(\boldsymbol{x},\boldsymbol{x}_0)\sigma_{ik}(\boldsymbol{x}) - \mu u_i(\boldsymbol{x})T^\epsilon_{ijk}(\boldsymbol{x},\boldsymbol{x}_0)\right)dV(\boldsymbol{x}) = \int_\Omega u_j(\boldsymbol{x})\phi_\epsilon(\boldsymbol{x}-\boldsymbol{x}_0)dV(\boldsymbol{x}),$$

which contains the *nonsingular* kernels S^ϵ and T^ϵ. Using the divergence theorem we write

$$\frac{1}{8\pi\mu}\int_{\partial\Omega}\left(S^\epsilon_{ij}(\boldsymbol{x},\boldsymbol{x}_0)\sigma_{ik}(\boldsymbol{x})n_k - \mu u_i(\boldsymbol{x})T^\epsilon_{ijk}(\boldsymbol{x},\boldsymbol{x}_0)n_k\right)ds(\boldsymbol{x}) = \int_\Omega u_j(\boldsymbol{x})\phi_\epsilon(\boldsymbol{x}-\boldsymbol{x}_0)dV(\boldsymbol{x}),$$

where $\boldsymbol{n}$ is the outward unit vector normal to the boundary $\partial\Omega$. The boundary $\partial\Omega$ includes the boundary ∂D of the solid body as well as the boundary of the ball containing D. Taking the limit as the radius of this ball tends to infinity, we find that the only contributions to the surface integral above that remain are the ones from the surface of D. Then one can write the last equation in terms of the boundary traction $f_i = -\sigma_{ik}n_k$ (since the normal vector points into D) as

$$-\frac{1}{8\pi\mu}\int_{\partial D} S^\epsilon_{ij}(\boldsymbol{x},\boldsymbol{x}_0)f_i ds(\boldsymbol{x}) - \frac{1}{8\pi}\int_{\partial D} u_i(\boldsymbol{x})T^\epsilon_{ijk}(\boldsymbol{x},\boldsymbol{x}_0)n_k ds(\boldsymbol{x}) = \int_\Omega u_j(\boldsymbol{x})\phi_\epsilon(\boldsymbol{x}-\boldsymbol{x}_0)dV(\boldsymbol{x}). \quad (12)$$

For comparison, the usual derivation of the boundary integral formulation of Stokes flow is done using a point force instead of the regularized force used here. The result in the singular case, found in [11], is the formula

$$-\frac{1}{8\pi\mu}\int_{\partial D} S^0_{ij}(\boldsymbol{x},\boldsymbol{x}_0)f_i ds(\boldsymbol{x}) - \frac{1}{8\pi}\int_{\partial D} u_i(\boldsymbol{x})T^0_{ijk}(\boldsymbol{x},\boldsymbol{x}_0)n_k ds(\boldsymbol{x}) = u_j(\boldsymbol{x}_0), \quad (13)$$

which can also be obtained from Eq. (12) after taking the limit $\epsilon \to 0$ and passing the limit inside the integrals.

Since D represents a solid body, the velocity inside D must necessarily satisfy the zero-deformation condition

$$\frac{\partial u_i}{\partial x_k} + \frac{\partial u_k}{\partial x_i} = 0.$$

Consequently, the pressure p is constant inside D and the stress tensor inside the solid body reduces to a constant multiple of the identity matrix, $\sigma_{ik} = -p\delta_{ik}$. We conclude that for each j

$$\int_D \frac{\partial}{\partial x_k} \left(S_{ij}^{\epsilon}(\boldsymbol{x}, \boldsymbol{x}_0)\sigma_{ik}(\boldsymbol{x}) \right) dV(\boldsymbol{x}) = 0,$$

so that if we integrate Eq. (11) in the region D and use $-\boldsymbol{n}$ as the outward normal to D, we find that

$$\frac{1}{8\pi} \sum_{i,k=1}^{3} \int_{\partial D} u_i(\boldsymbol{x}) T_{ijk}^{\epsilon}(\boldsymbol{x}, \boldsymbol{x}_0) n_k ds(\boldsymbol{x}) = \int_D u_j(\boldsymbol{x}) \phi_\epsilon(\boldsymbol{x} - \boldsymbol{x}_0) dV(\boldsymbol{x}). \tag{14}$$

Adding Eq. (12) to Eq. (14) and using the continuity of the velocity on ∂D, we arrive at

$$\int_{\mathbb{R}^3} u_j(\boldsymbol{x}) \phi_\epsilon(\boldsymbol{x} - \boldsymbol{x}_0) dV(\boldsymbol{x}) = -\frac{1}{8\pi\mu} \int_{\partial D} S_{ij}^{\epsilon}(\boldsymbol{x}, \boldsymbol{x}_0) f_i ds(\boldsymbol{x}). \tag{15}$$

Eq. (15) is the formula that provides the basis for the method of regularized Stokeslets discussed next. We note that our numerical method computes the solution of Eq. (1a) based on elements of the form given in Eq. (2), where $\boldsymbol{g}$ is the Stokeslet strength. Since the Stokeslet strength represents force exerted by the body on the fluid, it has the opposite sign as the traction, $\boldsymbol{g} = -\boldsymbol{f}$.

We point out that, since the Green's function in Eq. (15) is regular, the formula is valid even if the traction is concentrated at a single point. Consider, for example, $\boldsymbol{z} \in \partial D$ and the traction given by $f_i(\boldsymbol{x}) = \tilde{f}_i \ \delta^{2D}(\boldsymbol{x} - \boldsymbol{z})$, where δ^{2D} is a two-dimensional Dirac delta. Then Eq. (15) implies that

$$\int_{\mathbb{R}^3} u_j(\boldsymbol{x}) \phi_\epsilon(\boldsymbol{x} - \boldsymbol{x}_0) dV(\boldsymbol{x}) = -\frac{1}{8\pi\mu} S_{ij}^{\epsilon}(\boldsymbol{z}, \boldsymbol{x}_0) \tilde{f}_i,$$

which is also a regular expression.

3 The Method of Regularized Stokeslets

In this section, we describe the numerical method and provide error analysis. The method is based on a simple discretization of Eq. (15). For N Stokeslets located along the surface of the solid body D, we approximate the fluid velocity at any point $\boldsymbol{x}_0$ with

$$u_j(\boldsymbol{x}_0) = \frac{1}{8\pi\mu}\sum_{n=1}^{N}\sum_{i=1}^{3} S_{ij}^{\epsilon}(\boldsymbol{x}_n, \boldsymbol{x}_0) g_{n,i}\ A_n \tag{16}$$

where $g_{n,i}$ is the ith component of the force on the fluid applied at $\boldsymbol{x}_n$ and A_n is the quadrature weight of the nth particle. In the rest of this section, we analyze the two types of errors associated with this approximation: the regularization error on the left side of the equation and the discretization error in the integral approximation.

A The regularization error

Comparing the left sides of Eq. (15) and Eq. (16), the error due to the regularization ϕ_ϵ is introduced in the approximation of the integral

$$\int_{\mathbb{R}^3} u_j(\boldsymbol{x})\phi_\epsilon(\boldsymbol{x}-\boldsymbol{x}_0)dV(\boldsymbol{x}) \tag{17}$$

for the velocity $\boldsymbol{u}$ which is continuous across the boundary ∂D but whose gradient is typically discontinuous there. The order of the approximation of this integral depends on how far the evaluation point $\boldsymbol{x}_0$ is from ∂D. In this analysis we will use the specific cutoff in Eq. (9) although other cutoff functions can be designed based on the analysis. We note that for this radially symmetric cutoff we have

$$\int_{R_1<\|\boldsymbol{x}\|<R_2} \phi_\epsilon(\boldsymbol{x})d\boldsymbol{x} = 4\pi\int_{R_1}^{R_2} \frac{15\epsilon^4 r^2}{8\pi(r^2+\epsilon^2)^{7/2}}dr = \left.\frac{r^3(2r^2+5\epsilon^2)}{2(r^2+\epsilon^2)^{5/2}}\right|_{R_1}^{R_2}.$$

From this one can check that

$$\int_{R_1<\|\boldsymbol{x}\|} \phi_\epsilon(\boldsymbol{x})d\boldsymbol{x} \leq \epsilon^2 \quad \text{whenever} \quad R_c \equiv \sqrt{5\epsilon/2} \leq R_1.$$

This inequality shows that although the cutoff ϕ_ϵ has infinite support, most of its mass $(1-\epsilon^2)$ is concentrated in a ball of radius $R_c = \sqrt{5\epsilon/2}$. If the velocity components $u_j(\boldsymbol{x})$ satisfy $|u_j| < C$ and since the cutoff function is positive, we have that

$$\int_{\mathbb{R}^3} u_j(\boldsymbol{x})\phi_\epsilon(\boldsymbol{x}-\boldsymbol{x}_0)dV(\boldsymbol{x}) = \int_{\|\boldsymbol{x}\|\leq R_c} u_j(\boldsymbol{x})\phi_\epsilon(\boldsymbol{x}-\boldsymbol{x}_0)dV(\boldsymbol{x}) + O(\epsilon^2)$$

where $R_c = \sqrt{5\epsilon/2}$.

For any multi-index k, we define the kth moment of the cutoff as

$$M_{|k|}(\phi_\epsilon) = \int_{\mathbb{R}^3} \boldsymbol{x}^k \phi_\epsilon(\boldsymbol{x})d\boldsymbol{x}.$$

Since $\phi_\epsilon(\boldsymbol{x})$ is radially symmetric and scales like $\phi_\epsilon(\boldsymbol{x}) = \frac{1}{\epsilon^3}\phi_1(\boldsymbol{x}/\epsilon)$, we have that

$$M_{|k|}(\phi_\epsilon) = C_k \int_{\mathbb{R}^3} r^{k+2}\phi_\epsilon(r)dr = \epsilon^k \; M_{|k|}(\phi_1)$$

where $C_k = 0$ for $|k|$ odd due to symmetry.

We assume first that the field point $\boldsymbol{x}_0$ is located in the fluid such that $\text{dist}(\boldsymbol{x}_0, \partial D) > R_c$ and that the velocity $\boldsymbol{u}(\boldsymbol{x})$ is smooth enough in a ball of radius R_c centered at $\boldsymbol{x}_0$ for the following Taylor expansion to be valid

$$u_j(\boldsymbol{x}) = u_j(\boldsymbol{x}_0) + \sum_{k=1}^{3}(x_k - x_{0,k})\frac{\partial u_j(\boldsymbol{x}_0)}{\partial x_k} + \sum_{k,i=1}^{3}(x_k - x_{0,k})(x_i - x_{0,i})\frac{\partial^2 u_j(\boldsymbol{x}_0)}{\partial x_k \partial x_i} + O(\|\boldsymbol{x}-\boldsymbol{x}_0\|^3).$$

Then,

$$\begin{aligned}
&\int_{\|\boldsymbol{x}\|\le R_c} u_j(\boldsymbol{x})\phi_\epsilon(\boldsymbol{x}-\boldsymbol{x}_0)dV(\boldsymbol{x}) \\
= \;& u_j(\boldsymbol{x}_0)\int_{\|\boldsymbol{x}\|\le R_c}\phi_\epsilon(\boldsymbol{x}-\boldsymbol{x}_0)dV(\boldsymbol{x}) + \sum_{k,i}\frac{\partial^2 u_j}{\partial x_k \partial x_i}(\boldsymbol{x}_0)\int_{\|\boldsymbol{x}\|\le R_c} x_k x_i \phi_\epsilon(\boldsymbol{x})dV(\boldsymbol{x}) + O(\epsilon^2) \\
= \;& u_j(\boldsymbol{x}_0) + O(\epsilon^2),
\end{aligned}$$

where the first-order derivative terms do not appear due to the symmetry in $M_1(\phi_\epsilon)$. The equation indicates that the regularization error is $O(\epsilon^2)$ when $\mathrm{dist}(\boldsymbol{x}_0, \partial D) > R_c$.

When $\mathrm{dist}(\boldsymbol{x}_0, \partial D) < R_c$, the field point $\boldsymbol{x}_0$ is too close to the boundary of D and the Taylor expansion is not valid. Instead, one expansion is valid near $\boldsymbol{x}_0$ and outside of D, and a different expansion is valid near $\boldsymbol{x}_0$ and inside D. However, since u_j is continuous but its gradient is typically discontinuous across ∂D, the symmetry in $M_1(\phi_\epsilon)$ which eliminated the $O(\epsilon)$ error is no longer available and the regularization error is only $O(\epsilon)$ when $0 \le \mathrm{dist}(\boldsymbol{x}_0, \partial D) < R_c$.

B The discretization error

If we approximate the left-hand side of Eq. (15) with $u_j(\boldsymbol{x}_0)$, the equation reduces to a Fredholm equation of the first kind for the traction $\boldsymbol{f}$ for a given surface velocity. The kernel on the right side of Eq. (15) is nonsingular but its derivatives can be large and they enter into the estimate of the error in the quadrature Eq. (16).

Let a point $\boldsymbol{x} \in \partial D$ be described in Lagrangian form by $\boldsymbol{x} = \boldsymbol{X}(\boldsymbol{s}, t)$, where $\boldsymbol{s} = (s_1, s_2)$ is a material point on the surface. We assume that the surface ∂D can be covered by patches P_n for $n = 1, \ldots, N$ and that there is a smooth function that maps each patch to a rectangle such that the Jacobian of this map has no singular points. In this case, the integral on the right side of Eq. (15)

can be written in terms of the Stokeslets strengths as

$$\frac{1}{8\pi\mu}\int_{\partial D}\sum_{i=1}^{3}S_{ij}^{\epsilon}(\boldsymbol{x},\boldsymbol{x}_0)g_i ds(\boldsymbol{x}) = \frac{1}{8\pi\mu}\sum_{n=1}^{N}\int_{P_n}\sum_{i=1}^{3}S_{ij}^{\epsilon}(\boldsymbol{s},\boldsymbol{s}_0)g_i(\boldsymbol{s})J(\boldsymbol{s})d\boldsymbol{s}, \tag{18}$$

where $J(\boldsymbol{s}) = \left|\frac{\partial \boldsymbol{X}(\boldsymbol{s})}{\partial \boldsymbol{s}}\right|$ is the Jacobian of the transformation and $\boldsymbol{s}_0$ is the material point that corresponds to the evaluation point $\boldsymbol{x}_0$. The last integral can be approximated by any quadrature rule using points indexed by q within each patch, so that

$$\frac{1}{8\pi\mu}\int_{\partial D}\sum_{i=1}^{3}S_{ij}^{\epsilon}(\boldsymbol{x},\boldsymbol{x}_0)g_i ds(\boldsymbol{x}) \approx \frac{1}{8\pi\mu}\sum_{n=1}^{N}\sum_{i=1}^{3}\sum_{q}S_{ij}^{\epsilon}(\boldsymbol{s}_q,\boldsymbol{s}_0)g_i(\boldsymbol{s}_q)J(\boldsymbol{s}_q)(\Delta s_1\Delta s_2 w)_q, \tag{19}$$

where $(\Delta s_1\Delta s_2 w)_q$ represents the weight associated with point q in patch n. In the computations presented here we use the trapezoidal rule which requires estimates of the second derivatives of the integrand in order to find an error bound. For the two-dimensional trapezoidal rule, an error estimate on a single computational cell is given by

$$\iint_{cell}F(s_1,s_2)ds_1ds_2 - \frac{1}{4}\Delta s_1\Delta s_2\sum_{m,k=1}^{2}F(s_1^m,s_2^k) \approx \Delta s_1^3\Delta s_2(\partial^2F/\partial s_1^2) + \Delta s_1\Delta s_2^3(\partial^2F/\partial s_2^2), \tag{20}$$

where (s_1^m, s_2^k) represents the coordinates of the m,k corner of the cell, and

$$F(s_1,s_2) = S_{ij}^{\epsilon}(s_1,s_2,\boldsymbol{s}_0)g_i(s_1,s_2)J(s_1,s_2).$$

¿From the regularized Stokeslet formula, Eq. (10b), one can deduce that, if $\xi = \epsilon\boldsymbol{x}$,

$$S_{ij}^{\epsilon}(\boldsymbol{x},\boldsymbol{x}_0) = \frac{1}{\epsilon}S_{ij}^{\epsilon}(\xi,\xi_0),$$

and therefore

$$\frac{\partial S_{ij}^{\epsilon}(\boldsymbol{x},\boldsymbol{x}_0)}{\partial x_k} = \frac{1}{\epsilon^2}\frac{\partial S_{ij}^{\epsilon}(\xi,\xi_0)}{\partial \xi_k} \quad \text{and} \quad \frac{\partial^2 S_{ij}^{\epsilon}(\boldsymbol{x},\boldsymbol{x}_0)}{\partial x_k\partial x_m} = \frac{1}{\epsilon^3}\frac{\partial^2 S_{ij}^{\epsilon}(\xi,\xi_0)}{\partial \xi_k\partial \xi_m}.$$

Since the functions $S_{ij}^{\epsilon}(\xi,\xi_0)$, $\frac{\partial S_{ij}^{\epsilon}(\xi,\xi_0)}{\partial \xi_k}$ and $\frac{\partial S_{ij}^{\epsilon}(\xi,\xi_0)}{\partial \xi_k \partial \xi_m}$ are bounded and assuming $g_i(s_1,s_2)$ and $J(s_1,s_2)$ have bounded derivatives up to order two, the trapezoid rule error in Eq. (20) for a single computational cell is

$$Err = O\left(\Delta s_1^3 \Delta s_2 \left(\frac{C_1}{\epsilon} + \frac{C_2}{\epsilon^2} + \frac{C_3}{\epsilon^3}\right)\right) + O\left(\Delta s_1 \Delta s_2^3 \left(\frac{C_1}{\epsilon} + \frac{C_2}{\epsilon^2} + \frac{C_3}{\epsilon^3}\right)\right).$$

We mention that better estimates of quadrature formulas for weakly singular integrals have been derived elsewhere (see, for example, [12]). In order to estimate the global error, we multiply the local error for a single computational cell by the total number of computational cells, and conclude that the method of regularized Stokeslets in Eq. (16) approximates Eq. (15) with accuracy

$$O\left(\frac{\Delta s_1^2}{\epsilon^3}\right) + O\left(\frac{\Delta s_2^2}{\epsilon^3}\right) + O(\epsilon^q) \tag{21}$$

with $q = 1$ at evaluation points $\boldsymbol{x}_0$ on or near the boundary ∂D and with $q = 2$ at points sufficiently far from ∂D.

C Verification of rigid body motion

We expect that if the boundary of a closed fluid domain moves with the velocity of a rigid body in Stokes flow, then the entire enclosed region will move as a rigid body. In this section, we verify this analytically. In the next section, we present numerical evidence that the fluid velocity field inside a translating sphere, computed using regularized Stokeslets, is consistent with rigid body motion.

Our numerical method is based on the Lorentz reciprocal identity Eq. (11). When applied to a fluid domain D, the identity yields

$$\frac{1}{8\pi\mu}\int_{\partial D} S_{ij}^{\epsilon}(\boldsymbol{x},\boldsymbol{x}_0) f_i ds(\boldsymbol{x}) + \frac{1}{8\pi}\int_{\partial D} u_i(\boldsymbol{x}) T_{ijk}^{\epsilon}(\boldsymbol{x},\boldsymbol{x}_0) n_k ds(\boldsymbol{x}) = \int_D u_j(\boldsymbol{x})\phi_\epsilon(\boldsymbol{x}-\boldsymbol{x}_0) dV(\boldsymbol{x}). \tag{22}$$

Now suppose $\mathbf{U}$ and $\mathbf{\Omega}$ are constant vectors. Based on Eq. (5a), (5b), and Eq. (8), we find that

$$\frac{\partial T^{\epsilon}_{ijk}(\boldsymbol{x},\boldsymbol{x}_0)}{\partial x_k} = -8\pi\delta_{ij}\phi_\epsilon(\boldsymbol{x}-\boldsymbol{x}_0)$$

and

$$\frac{\partial}{\partial x_k}[(\mathbf{\Omega}\times\boldsymbol{x})_i T^{\epsilon}_{ijk}(\boldsymbol{x},\boldsymbol{x}_0)] = -8\pi(\mathbf{\Omega}\times\boldsymbol{x})_j\phi_\epsilon(\boldsymbol{x}-\boldsymbol{x}_0).$$

These equations can be used to prove that if the boundary velocity of the fluid volume D is consistent with rigid-body motion, $\boldsymbol{u}^b = \mathbf{U} + \mathbf{\Omega}\times(\boldsymbol{x}-\boldsymbol{x}_c)$, then the corresponding traction is $f^b_i = -\sigma_{ij}n_j = pn_i$ and the following identities can be established

$$\begin{aligned}\int_{\partial D} S^{\epsilon}_{ij}(\boldsymbol{x},\boldsymbol{x}_0) f^b_i ds(\boldsymbol{x}) &= 0,\\ \int_{\partial D} u^b_i(\boldsymbol{x}) T^{\epsilon}_{ijk}(\boldsymbol{x},\boldsymbol{x}_0) n_k ds(\boldsymbol{x}) &= 8\pi\int_D u^b_j(\boldsymbol{x})\phi_\epsilon(\boldsymbol{x}-\boldsymbol{x}_0)d\boldsymbol{x}.\end{aligned}$$

We note that the integral on the right-hand side of the last equation is approximately equatl to $u^b_i(\boldsymbol{x}_0)$ when $\boldsymbol{x}_0$ is well inside D (as long as the support of ϕ_ϵ is inside D), it equals 0 when $\boldsymbol{x}_0$ is well outside D and is approximately $\frac{1}{2}u^b_i(\boldsymbol{x}_0)$ when $\boldsymbol{x}_0$ is on the boundary since the integral includes about half of the support of ϕ_ϵ.

Eq. (22) then reduces to

$$\int_D u^b_i(\boldsymbol{x})\phi_\epsilon(\boldsymbol{x}-\boldsymbol{x}_0)d\boldsymbol{x} = \int_D u_j(\boldsymbol{x})\phi_\epsilon(\boldsymbol{x}-\boldsymbol{x}_0)dV(\boldsymbol{x}). \tag{23}$$

This shows that $u_j(\boldsymbol{x}_0) = u^b_j(\boldsymbol{x}_0)$ for points inside D on account of the arbitrariness of the support of ϕ_ϵ.

4 Example 1: Translating sphere

Consider the fluid motion produced by a solid sphere of radius a translating with velocity $\mathbf{U} = (0,0,U_3)^T$ in a Stokes flow of viscosity μ. The exact solution for the velocity field $\boldsymbol{u} = (u_1,u_2,u_3)^T$

at a point $\boldsymbol{x} = (x_1, x_2, x_3)^T$ outside the sphere is (see, for instance, [13]):

$$\begin{aligned} u_1(x_1, x_2, x_3) &= \frac{3aU_3}{4}\left(\frac{1}{r^3} - \frac{a^2}{r^5}\right) x_1 x_3 \\ u_2(x_1, x_2, x_3) &= \frac{3aU_3}{4}\left(\frac{1}{r^3} - \frac{a^2}{r^5}\right) x_2 x_3 \\ u_3(x_1, x_2, x_3) &= \frac{3aU_3}{4}\left(\frac{1}{r^3} - \frac{a^2}{r^5}\right) x_3^2 + \frac{aU_3}{4r}\left(3 + \frac{a^2}{r^2}\right) \\ p(x_1, x_2, x_3) &= p_0 + \frac{3}{2}\frac{aU_3 x_3}{r^3}. \end{aligned} \tag{24}$$

Here r is the distance from the point $\boldsymbol{x}$ to the center of the sphere. Note that, inside the solid sphere, the velocity is $\mathbf{U} = (0, 0, U_3)^T$. The hydrodynamic traction on the sphere is:

$$\boldsymbol{f}(\boldsymbol{x}) = -\frac{3\mu}{2a}\mathbf{U}. \tag{25}$$

The traction on a translating sphere is indeed independent of position. This is only true for a sphere due to symmetry.

In order to apply the method of regularized Stokeslets to this test problem, we discretize the surface of the unit sphere ($a = 1$) using a six-patch structured grid. It is constructed by placing the sphere inside a cube with an $N \times N$ uniform grid on each face. The computational grid results from the intersection of sphere's surface with lines joining the center of the sphere and the nodes on the cube [11]. In this way, the approximate grid size on the sphere is $\Delta s = 2\pi a/4N$. At each of the points on the surface, we apply the force in Eq. (25). Using Eq. (16), we can compute the resulting velocity at the points on the surface, and compare it to the exact solution $(0, 0, U_3)^T$.

We examine the errors in the third component of surface velocity with $U_3 = -1$. Figure 2 shows the dependence of the $L2$-norm of the surface velocity error on the regularization parameter

ϵ for a fixed six-patch grid, 24×24 points on each patch. This gives a discretization size of about $\Delta s = 0.065$. Note that for large values of ϵ the error grows linearly and as ϵ is reduced, the error initially decreases but is ultimately overtaken by the increasing quadrature error, as suggested by the error bound in Eq. (21).

Figure 3 shows the $L2$-norm of the surface velocity error for a fixed ϵ as the grid is refined, from a six patch 12×12 grid down to a six patch 192×192 grid. Note that for the three finest grids, the regularization error dominates, and the finer discretization is not advantageous. For the coarser grids, the quadratic dependence on Δs is apparent.

Figure 4 shows the quadrature error in the computation of the surface integral in Eq. (19) at two points $\boldsymbol{x}_0$ for various $\Delta s = \Delta s_1 = \Delta s_2$ and fixed $\epsilon = 0.01$. The bottom dashed line is the error at a point on the surface of the sphere. The top dashed line is the error at a point half a radius outside the sphere. The exact value of the velocity is given by the surface integral on the right side of Eq. (15) which can also be obtained accurately by computing the volume integral on the left side of Eq. (15). We do this numerically using a very fine grid and the exact velocity field in Eq. (24).

Figure 5 shows the error in the computed velocity as a function of the regularization parameter ϵ at both a point on the surface of the sphere (top graph) and a point in the exterior of the sphere far from the surface (bottom graph). Note that on the surface of the sphere this error increases linearly for large values of ϵ. The point corresponding to $\epsilon = 0$ was computed by avoiding placing a force vector at the evaluation point. The bottom graph shows the velocity error at a point farther from the sphere where the computation is more accurate. These errors are smaller in magnitude and depend quadratically on ϵ as the analysis in the previous sections indicates. For small values of ϵ, the discretization errors dominate and are nonzero since the grid is fixed.

We verified that the velocity field given by our model inside the sphere is consistent with solid body motion. We imposed the surface boundary condition to be the velocity $\mathbf{U} + \boldsymbol{x} \times \boldsymbol{\Omega}$, where $\mathbf{U} = (0, 0, 1)^T$ and $\boldsymbol{\Omega} = (0, 0, 1)^T$. This represents translation and rotation of the surface of the sphere. Given this surface velocity, we computed the corresponding Stokeslets strengths as described in the next section and used them to compute the velocity field on the plane $z = 0.2$ inside the sphere. The z-component of the velocity field at all points was $1 \pm 4 \times 10^{-4}$, giving the correct rate of translation. The radial component of the xy-velocity of all points was $\pm 1 \times 10^{-5}$, indicating that, in addition to the translation, the plane $z = 0.2$ inside the sphere simply rotates. The rotational velocity of all points $(x, y, 0.2)$ was computed to be $1 \pm 5 \times 10^{-4}$ times $\sqrt{x^2 + y^2}$, indicating the correct angular velocity.

A Computation of resistance matrices for a sphere

In this section, we discuss the computation of resistance matrices that describe the linear relationship between the total hydrodynamic force and torque and the translational and angular velocities of a rigid body moving in a Stokes flow. We compare the resistance matrices generated by the method of regularized Stokeslets for a moving sphere to those known from classical theory.

The total hydrodynamic force exerted on the solid whose boundary experiences the traction $\boldsymbol{f}$ is:

$$\mathbf{F} = \int_{\partial D} \boldsymbol{f}(\boldsymbol{x}) \; ds(\boldsymbol{x}) \tag{26}$$

and the total hydrodynamic torque is given by:

$$\mathbf{L} = \int_{\partial D} \boldsymbol{x} \times \boldsymbol{f}(\boldsymbol{x}) \; ds(\boldsymbol{x}). \tag{27}$$

In the case of a rigid body, we decompose the force into a drag force due to translational motion

of the body, and a force due to rotation of the body. The linearity of the Stokes equations allows us to represent these forces in terms of resistance matrices acting on the velocity $\mathbf{U}$ and angular velocity $\mathbf{\Omega}$ vectors of the rigid motion [1]:

$$\mathbf{F} = -\mu(\mathcal{T}\ \mathbf{U} + \mathcal{P}\ \mathbf{\Omega}) \tag{28}$$

$$\mathbf{L} = -\mu(\mathcal{P}^T\ \mathbf{U} + \mathcal{R}\ \mathbf{\Omega}). \tag{29}$$

Here $\mathcal{T}$, $\mathcal{P}$, nd $\mathcal{R}$ are 3×3 resistance matrices that depend only upon the geometry of the solid body.

In the case of a sphere, it is apparent due to symmetry that the translation and rotation resistance matrices $\mathcal{T}$ and $\mathcal{R}$ are constant multiples of the identity, and that $\mathcal{P} = 0$. In fact, one can easily compute the total hydrodynamic force $\mathbf{F}$ induced by a translating sphere with constant velocity $\mathbf{U}$ by integrating the traction in Eq. (25) over the surface of the sphere to get the classical result $\mathbf{F} = -6\pi\mu a\mathbf{U}$. In the case of a sphere rotating about its center with angular velocity $\mathbf{\Omega}$, the total hydrodynamic torque is $\mathbf{L} = -8\pi\mu a^3\mathbf{\Omega}$. Therefore, the resistance matrices for a sphere of radius a are $\mathcal{T} = 6\pi a\mathcal{I}$ and $\mathcal{R} = 8\pi a^3\mathcal{I}$.

The method of regularized Stokeslets has been presented as a way to compute the velocity field in Stokes flow resulting from a given distribution of forces localized at a set of points. Consider the discretization of the surface of an object by the points $\boldsymbol{x}_1, \boldsymbol{x}_2, \ldots, \boldsymbol{x}_N$, and consider Stokeslets of strength $\boldsymbol{g}_1, \boldsymbol{g}_2, \ldots, \boldsymbol{g}_N$ applied at these points. The linear relationship between the velocities and the forces at these points may be calculated from (16):

$$u_{m,j} = \frac{1}{8\pi\mu}\sum_{n=1}^{N}\sum_{i=1}^{3} S_{ij}^{\epsilon}(\boldsymbol{x}_n, \boldsymbol{x}_m) g_{n,i}\ A_n. \tag{30}$$

Here $\boldsymbol{g}_n = (g_{n,1}, g_{n,2}, g_{n,3})^T$, $j = 1, 2, 3$ and $m = 1, \ldots, N$. We may write this relationship in matrix

vector form:

$$\boldsymbol{u} = \frac{1}{8\pi\mu}\mathcal{A}\boldsymbol{g}, \tag{31}$$

where the vectors of length $3N$ are $\boldsymbol{u} = (\boldsymbol{u}_1, \boldsymbol{u}_2, \ldots, \boldsymbol{u}_N)^T$ and $\boldsymbol{g} = (\boldsymbol{g}_1, \boldsymbol{g}_2, \ldots, \boldsymbol{g}_N)^T$, and $\mathcal{A}$ is a $3N \times 3N$ matrix whose entries depend upon the coordinates $\boldsymbol{x}_1, \boldsymbol{x}_2, ..., \boldsymbol{x}_N$, the regularization parameter ϵ and the surface discretization.

Conversely, one may also use the linear relationship in Eq. (31) to compute the Stokeslet strengths that generate a specified velocity of the solid body. The matrix $\mathcal{A}$ is a discretization of the single-layer potential on the right side of Eq. (15) which is known not to be invertible in general. For example, consider a normal force of constant magnitude applied to the surface of a sphere. This pressure-like force will not cause any fluid motion due to the incompressibility in Eq. (5b) regardless of the magnitude of the forces. In algebraic terms, the matrix $\mathcal{A}$ has a nontrivial null-space and therefore, a unique solution of Eq. (31) is not guaranteed. For the computation of the total force $\mathbf{F}$ in Eq. (28) on the surface of the sphere, this is not a problem since the symmetry of the sphere implies that forces of the form $\boldsymbol{g}(\boldsymbol{x}) = c\boldsymbol{n}(\boldsymbol{x})$ will have no contribution to the value of $\mathbf{F}$. In our computation of the Stokeslets $\boldsymbol{g}$ from Eq. (30), we found that using the iterative procedure GMRES with zero initial guess works well.

In order to illustrate how the method of regularized Stokeslets can be used to assemble the resistance matrices $\mathcal{T}, \mathcal{P}$ and $\mathcal{R}$, we apply a constant velocity of $\boldsymbol{u}_j = (1, 0, 0)^T$ to each point $\boldsymbol{x}_j, j = 1, 2, ..., N$ on the surface of the solid, in a fluid of viscosity $\mu = 1$. We then use Eq. (31) to solve for the Stokeslet strengths $\boldsymbol{g}$. The traction then is given by $\mathbf{f} = -\boldsymbol{g}$. The traction is integrated over the boundary to arrive at the total hydrodynamic force vector $\mathbf{F}$. However, in this case $\mathbf{U} = (1, 0, 0)^T$, and $\boldsymbol{\Omega} = \mathbf{0}$. Using Eq. (28), the entries of the first column of the translation

resistance matrix $\mathcal{T}$ must be equal to the total hydrodynamic force $\mathbf{F}$. Similarly, the first column of the resistance matrix $\mathcal{P}^T$ must be equal to the total hydrodynamic torque computed by integrating $\boldsymbol{x}_j \times \boldsymbol{f}_j, j = 1, 2, \ldots, N$ over the boundary (see Eq. (29)). The remaining columns of $\mathcal{T}$ and $\mathcal{P}^T$ are computed by applying translational velocities in the other two coordinate directions, and using Eq. (31) to solve for the forces. A systematic application of rigid rotations about each of the three coordinate axes enables us to assemble the rotational resistance matrix $\mathcal{R}$.

We calculate the resistance matrices for a sphere of radius $a = 1$, where our discretization used a six-patch grid, 48×48 points on each face, and a regularization parameter $\epsilon = 0.01$. For these values, the analytical solution for these matrices is $\mathcal{T} = 6\pi\mathcal{I} \approx 18.85\ \mathcal{I}$, $\mathcal{R} = 8\pi\mathcal{I} \approx 25.133\ \mathcal{I}$, and $\mathcal{P} = 0$. The computed values of the matrices are

$$\mathcal{T} = \begin{pmatrix} 18.80 & 1.3 \times 10^{-9} & -6.7 \times 10^{-10} \\ -9.8 \times 10^{-10} & 18.80 & -2.5 \times 10^{-11} \\ -7.1 \times 10^{-10} & 1.5 \times 10^{-10} & 18.80 \end{pmatrix}$$

$$\mathcal{P}^{\mathcal{T}} = \begin{pmatrix} -3.3 \times 10^{-10} & -1.6 \times 10^{-9} & -2.3 \times 10^{-9} \\ -1.4 \times 10^{-10} & 1.5 \times 10^{-11} & 1.2 \times 10^{-10} \\ 5.3 \times 10^{-10} & 3.9 \times 10^{-10} & 1.9 \times 10^{-11} \end{pmatrix}$$

$$\mathcal{P} = \begin{pmatrix} -1.6 \times 10^{-9} & 1.2 \times 10^{-9} & 1.8 \times 10^{-10} \\ 4.0 \times 10^{-9} & -1.0 \times 10^{-9} & -2.2 \times 10^{-8} \\ -5.1 \times 10^{-9} & 1.2 \times 10^{-8} & -7.0 \times 10^{-9} \end{pmatrix}$$

$$\mathcal{R} = \begin{pmatrix} 25.09 & 4.1 \times 10^{-11} & 1.2 \times 10^{-10} \\ 4.0 \times 10^{-10} & 25.09 & -2.2 \times 10^{-9} \\ -1.0 \times 10^{-10} & -3.8 \times 10^{-10} & 25.09 \end{pmatrix}.$$

Since the method of regularized Stokeslets has been applied to points on the surface of the sphere, we expect the error in the computation to be $O(\epsilon)$ in addition to errors in the iterative solver and the computation of the global quantities. The off-diagonal entries of the matrices show very little error while the nonzero diagonal entries show an error of about 5ϵ.

Table 1 presents the convergence of the diagonal values of $\mathcal{T}$ as the regularization and discretization parameters are refined. By looking at the last column, corresponding to the finest grid, one can appreciate the linear convergence in ϵ. On the other hand, by looking at the row corresponding to $\epsilon = 0.01$, one can see the convergence as the discretization size is reduced. Table 2 presents similar convergence results for $\mathcal{R}$.

5 Motion of a rigid helical body

In this section, we consider a rigid helical tube of nonzero thickness in a viscous fluid. We present comparisons of our numerical results with experimental results on two related test problems based upon this helical geometry: (a) computation of resistance coefficients for helical tubes, and (b) computation of the forward progression of a rigid helix due to an externally imposed torque.

A Resistance coefficients

In Stokes flow, the linear relationships in Eq. (28)-(29) between forces and torques and translational and angular velocities of a rigid object involve resistance matrices whose entries *depend only upon the geometry* of the object. Purcell [14] designed a physical experiment that could be used to back out these resistance coefficients. A helical wire was dropped under its own weight into silicon oil. The experiments measured the wire's sinking speed and rate of rotation, and then used those values to estimate the resistance coefficients from mathematical formulas. In particular, the force, the linear velocity and the angular velocity were assumed to point in the direction of the helix axis, which is equivalent to reducing Eq. (28)-(29) to scalar equations relating the vector magnitudes linearly with proportionality constants $-\mu\mathcal{T}_{33}$, $-\mu\mathcal{P}_{33}$ and $-\mu\mathcal{R}_{33}$ (since the axes of the helices are

assumed to be aligned with the z-axis). The specified helix parameters were L, the ratio L/λ and the pitch angle ϕ defined by

$$\tan\phi = \frac{2\pi R}{\lambda}.$$

The helix radius R was allowed to vary in order to design the helices that fit the other parameters. Results deduced from Purcell's experiments recorded in a lab notebook were included in [14], and are shown in Table 3. However, there was no information specified on the thickness of the wires used in these experiments.

For comparison, we use the method of Regularized Stokeslets to calculate the resistance coefficients of the helical tubes, as we did for the sphere in the previous section. Although our numerical experiments involve external forces as well as externally applied torques that do not exist in Purcell's experiment of a sinking wire, the resistance matrices should, nevertheless, be equivalent, since the entries depend only upon the geometry of the helical tube. We designed helical tubes with parameters similar to those specified in [14]. The tube is constructed based on a helical centerline (x_c, y_c, z_c) given by

$$x_c(s) = R\cos(2\pi z_c/\lambda), \qquad y_c(s) = R\sin(2\pi z_c/\lambda), \qquad 0 \le z_c \le L$$

where R is the radius of the helix and λ is the pitch. We consider only helices where L is an integer multiple of λ. We assume that each cross-section is circular with radius a, representing the thickness of the tube. This tube is discretized with M cross-sections along its length with N points each.

We performed computations with a range of thickness parameters, and found good agreement with the experimental data for helical tubes with diameters in the range of about $0.5 - 1.0$ mm, equivalent to $18 - 24$ US standard gauge wire. We present results for a helical tube diameter of

$a = 0.025$ cm in Table 4. The regularization parameter was set to $\epsilon = 0.01$ and we computed the corresponding resistance coefficients as described previously for a grid consisting of 400 cross-sections and 6 points per cross-section.

The resistance coefficients in Table 4 compare very well with the experimental values in Table 3 for all of the parameter combinations. To assess the effect of the tube's discretization, we chose the parameters associated with the first row of Table 4 and we computed the corresponding resistance coefficients for two grids of different levels of refinement while keeping $\epsilon = 0.01$. The results in Table 5 show additional improvement in the agreement with finer discretizations.

B Rigid Helix - externally imposed torque

Spirochetes are an order of bacteria characterized by a unique cellular anatomy and mode of motility [15, 6], and include the causative agents of syphilis and Lyme disease. The locomotory ability of these pathogenic spirochetes enables them to screw through viscous fluids and mucosal surfaces. The method of locomotion of these bacteria that lack external flagella has been puzzling. Their helical shape is imparted to them by a rigid protoplasmic cylinder. This cylinder is surrounded by a membrane referred to as the outer sheath. The region between the outer sheath and the cytoplasmic membrane is termed the periplasmic space. Within this region are a number of internal or periplasmic flagella that attach at either tip of the protoplasmic cylinder. There is evidence that these periplasmic flagella rotate in a manner similar to other bacteria [16]. The rotation of these periplasmic flagella cause the spirochete to swim.

Berg [17] proposed a model for spirochete motion in which he showed that an external flagellum was not needed to produce the torque required to propel the helical cell. He assumed that the

protoplasmic cylinder is semi-rigid, that the periplasmic flagella rotate in the same manner as external flagella of other bacteria, and that the outer sheath is flexible and free to rotate about the protoplasmic cylinder. However, there is evidence, at least in *Leptospira*, that the outer sheath is quite fluid [18], suggesting that it might not rotate as a single sheet. Ignoring the internal structure of the cells, Lighthill [2, 19] used a slender body approximation to analyze the fluid velocity field in the vicinity of swimming spirochetes using helical distributions of Stokeslets and dipoles. As discussed above, Purcell [14] later examined the relationship between forces and torques and velocities of rotating helical objects in a viscous fluid.

In order to gain insight into spirochete motility, we turn to the steady state rotational motion of a finite length, finite body width, helix. We have demonstrated that we can use the method of regularized Stokeslets to calculate resistance matrices for solid objects that describe the linear relationship between drag and rotational velocities and total force. No restrictive assumptions about these solid objects need to be made, such as slender bodies or small amplitude waveforms. For a given helical geometry and width of the body, we would like to compute the ratio between angular speed ($|\omega|$) of the turning helix and the forward tranlational speed ($|v|$). This is done as follows. Once we have calculated the resistance coefficients in the manner of the previous section, we set the total force $\mathbf{F}$ in Eq. (28) to zero as a requirement for steady state motion (no acceleration). We assume that the linear velocity and angular velocity are in the direction of the helix axis which is aligned with the z-axis. Therefore, the ratio $|\omega/v| = |\mathcal{T}_{33}/\mathcal{P}_{33}|$.

We performed a set of experiments on helical geometries, some of which are shown in Figure 6. Using experimental data for *Leptonema illini* [15, 16], we chose a body length of 11.93 μm, and a body radius of 0.0735 μm, and a helix radius of 0.088 μm. As shown in Figure 6, we varied the

number of pitches per body length, keeping the other helix and geometrical parameters fixed. Once we computed the ratio of angular velocity to translational velocity we determined the number of rotations required for the organism to progress one body length. Figure 7 shows the number of rotations as a function of the number of pitches per body length. If one considers this a measure of swimming efficiency, we see that either too few pitches or too many are less efficient than the mid-range values of $10 - 18$ pitches per body length. In fact, the average pitch of *L. illini*, is $0.702\ \mu m$, which would be 17 pitches per body length, which falls in this range. Figure 8 shows a high-voltage transmission photograph of a *Leptonema illini*. Our calculations indicate that such an organism would require roughly 128 rotations to progress one body length. In recent experiments of motile *L. illini* in buffer solution, free of polymers, Goldstein [20] reports that for a body length of $12\mu m$, the number of turns the body makes in order to swim one body length is about 140. These data were taken on a sample of eight cells, and the standard deviation from the average of 140 turns is 13. This range is shown as an error bar in Figure 7.

6 Motion of an elastic helical body

In this section we briefly describe the modeling of a non-rigid, dynamically rotating helix in a viscous fluid using the regularized Stokeslet method. As a first step in capturing the fluid-structure interactions between a spirochete and the surrounding fluid, we have developed an elastic model of a helix with rotation driven by internal motors.

We choose an immersed boundary representation, where the outer sheath of the spirochete is modeled by a discrete collection of points that are interconnected by springs (see, for instance [21, 22, 23]). Circles of points are placed regularly about a centerline along the length of the helix,

in planes normal to the centerline. A series of springs around the circular cross-sections can be thought of as forming circular filaments or fibers. Similarly, other series of springs connecting the discrete points form longitudinal and right- and left-handed helical filaments. In order to model the helical shape, the resting lengths of these springs are held at their lengths at the start of the simulation. We may vary the elastic properties of the outer sheath by varying the stiffness constants of the springs that form each family of filaments.

In order to generate rotation of the helix while conserving momentum and angular momentum, we add internal *motor springs* that connect rings on the outer sheath to inner structural rings at segments on either end of the helix. The rotation will be driven by the contraction of these dynamic springs (see Figure 9). As the springs between the rings contract, these rings will counter-rotate, causing the entire structure to rotate. When the tension of a spring falls below a given tolerance, the spring is reformed with an attachment point further away on the outer sheath ring. We think of the space between the rings as the periplasmic space between the cell body and outer sheath in a true spirochete. In this model, we do not explicitly represent the internal periplasmic flagella, but their action is modeled by the distribution of the motor springs. The rotation speed of the entire structure is not preset, but is determined by the stiffness constants of the motor springs and structural springs, along with the tension tolerance imposed. These dynamics springs are analogous to those used to model the molecular motor dynein acting upon microtubules in eukaryotic cilia [21].

Our immersed boundary helical structure is coupled to the surrounding viscous incompressible fluid in the following manner. At the beginning of a time step, the state of the system is determined by the configuration of the discrete set of material points that make up the outer sheath and the

inner rings of the model spirochete. The restoring forces due to each of the structural springs and motor springs contribute to resultant forces $\boldsymbol{g}_n$ acting on the fluid at each material point $\mathbf{x}_n$. These forces are used to determine the velocity at each discrete point using the summation in Eq. (16). These velocities are used to update the positions of the material points using a high-order integration scheme [24].

Note that although the Stokes equations are steady, time-dependence appears in this model due to evolution of the spring forces as the configuration of the material points change. The geometry of the model spirochete can vary as it responds to the motion of the viscous fluid. Likewise, the motion of the fluid is determined by the action of the structural elastic forces and the motor forces applied at the either end of the model organism.

We illustrate the capability of this model in Figure 10, which shows a sequence of snapshots of a model spirochete at equally spaced time intervals. The left-most frame in Figure 10 shows the regular geometry of this helical structure at the start of the simulation, when all the structural springs that build the spirochete are at their rest lengths. Here the body length is 6 times the pitch (see Figure 10). The discretization of the surface includes 100 rings and 8 points per ring. Five internal motor rings are placed within each end of the helix, and motor springs under tension are activated at the start of the simulation. The dynamic action of these motor springs that attach, break, and reattach to points on the outer rings generate a steady rotation of the structure. Figure 10 show that these rotations result in steady progress in the swimming direction. In fact, the swimming speed measured in these dynamic calculations is very close to the swimming speed measured for a rigid helix with the same geometry using the steady state model described earlier.

Although large stiffness constants have been used for the structural springs, one can note the

slight change in the shape of the helix from the initial frame to the last. In particular, note that the pitch-length is no longer constant in the last frame. The helix is elongated at the bottom, and somewhat compressed at the top as it experiences resistance from the viscous fluid. We may also evaluate the flow field at any point in space using Eq. (16). Figure 11 shows a snapshot of the velocity field along a transverse plane to the helical structure at a fixed time step.

7 Conclusion

We have presented the method of regularized Stokeslets for the numerical computation of Stokes flows in three dimensions driven by body forces applied along moving boundaries. The method had been presented previously [5] for two-dimensional problems, although the accuracy of the method had been demonstrated only numerically. The method of regularized Stokeslets is based on the superposition of exact solutions of the Stokes equations when forces are given by a cutoff function. In cases when the forces are distributed over a surface, the method is interpreted as a discretization of a boundary integral, similar to a boundary element method. However, the points where the forces are applied need not discretize a smooth surface; they may represent a curve in three dimensions or a collection of randomly distributed points. In these cases, the regularization parameter plays the role of a physical parameter that merely gives the extent of the region where the force is applied since the limit as $\epsilon \to 0$ of the resulting velocity does not exist.

Our analysis of the accuracy of the method of regularized Stokeslets shows that when the forces are on surfaces, part of the error is due to the regularization and depends only on the cutoff parameter ϵ. Another part of the error is due to the discretization of the surface integral and depends on ϵ as well as the discretization parameters. The regularization error is shown to be $O(\epsilon)$

in a region of size $O(\sqrt{\epsilon})$ surrounding the moving boundaries but the error improves to $O(\epsilon^2)$ away from the boundaries. For a fixed discretization, the discretization error is inversely proportional to a power of ϵ, making it possible to find an optimal value of the regularization parameter.

The results of the analysis were validated using two test problems. The well-known flow around a sphere was used to evaluate the performance of the method and the errors inside the sphere as well as at positions near and far from the boundary of the sphere. The calculations agree with the analysis. The formula that relates the velocity of the particles to the force applied at them can be used to compute the force required to generate a given velocity; that is, it can be used to impose a velocity boundary condition. Assuming a linear dependence of the force and torque on velocity, resistance matrices for the sphere were computed and compared with known analytical values. The results show that as the numerical parameters are refined, the computed values are within the error estimates of the exact values.

A second test problem was that of the solid-body motion of a helical tube. The computed resistance coefficients were compared with the experimental data obtained by Purcell [14] for helical tubes of various lengths, pitches, and pitch angles. Although the thickness of the wires used in the experiments was not known, most of the coefficients computed were within 10% of the reported values.

In addition, using the geometrical data obtained for *Leptonema illini* along with our method for computing resistance matrices, we numerically estimated the ratio of angular speed to swimming (linear) speed of these spirochetes. The ratio was computed for helices of fixed body length (viewed from the side), fixed helical diameter and fixed body radius, but with the number of pitches per body length varied. Our calculations show that this ratio is minimum (indicating higher swimming

efficiency), for pitch lengths in the range 0.6628–1.193 μm. This range includes the *L. illini* average pitch length of 0.702 μm [15].

Finally, we have presented a dynamic computation of the motion of an elastic helical tube driven by internal motors. This example illustrates how the coupling of the passive elastic properties of the body, active internal force generation and fluid motion may be achieved. We will use this methodology in future work to build models that encompass increasing levels of detail of the internal structure and physiology of spirochetes.

8 Acknowledgements

This work was supported by the National Science Foundation Grant DMS-0201063. Computations were performed at the Center for Computational Science at Tulane and Xavier Universities, supported by the US Department of Energy contract DE-FG02-01ER63119.

References

[1] C. Pozrikidis, 1992. Boundary Integral and Singularity Methods for Linearized Viscous Flow. Cambridge University Press.

[2] M. J. Lighthill, 1976. Flagellar hydrodynamics. SIAM Rev., v. 18, pp. 161-230.

[3] J. B. Keller and S. I. Rubinow, 1976. Slender-body theory for slow viscous flow. J. Fluid Mech., v. 75, pp. 705-714.

[4] M. Shelley and T. Ueda, 2000. The Stokesian hydrodynamics of flexing, stretching filaments. Phys. D., v. 146, pp. 221-245.

[5] R. Cortez, 2001. The method of regularized Stokeslets. SIAM J. Sci. Comput., v. 23, pp. 1204-1225.

[6] S. C. Holt, 1978. Anatomy and chemistry of the spirochetes. Microbiological Reviews, v. 42, pp. 114-160.

[7] Peskin, C.S., 2002. The immersed boundary method. Acta Numerica, 11:479-517.

[8] J. T. Beale and A. Majda, 1985. High Order Accurate Vortex Methods With Explicit Velocity Kernels. J. Comput. Phys., v. 58, pp. 188.

[9] O. H. Hald, 1991. Convergence of Vortex Methods, in "Vortex Methods and Vortex Motion" (K. E. Gustafson and J. A. Sethian, Eds.), pp. 33, (SIAM, Philadelphia).

[10] P. Degond and S. Mass-Gallic, 1989. The Weighted Particle Method for Convection-Diffusion Equations I: The Case of Isotropic Viscosity. Math. Comp., v. 53, pp. 485.

[11] C. Pozrikidis, 1998. Numerical Computation in Science and Engineering. Oxford Univ. Press, New York.

[12] J. T. Beale, 2001. A Convergent Boundary Integral Method for Three-Dimensional Water Waves. Math. Comp., v. 70, pp. 977-1029.

[13] G. K. Batchelor, 1967. An Introduction To Fluid Dynamics. Cambridge University Press.

[14] E. Purcell, 1997. The efficiency of propulsion by a rotating flagellum. Proc. Natl. Acad. Sci., v. 94, pp. 11307-11311.

[15] S. Goldstein and N. Charon, 1990. Multiple-exposure photographic analysis of a motile spirochete. Proc. Natl. Acad. Sci., v. 87, pp. 4895-4899.

[16] S. Goldstein, K. Buttle, and N. Charon, 1996. Structural analysis of the *Leptospiraceae* and *Borrelia burgdorferi* by high-voltage electron microscopy. J. of Bacteriology, v. 178, no. 22, pp. 6539-6545.

[17] H. C. Berg, 1976. How spirochetes may swim. J. Theor. Biol., v. 56, pp. 269-273.

[18] N. W. Charon, C.W. Lawrence and S. O' Brien, 1981. Movement of antibody-coated latex beads attached to the spirochete Leptospira interrogans. Proc. Natl. Acad. Sci. U.S.A., 78: p. 7166-7170.

[19] M. J. Lighthill, 1996. Helical distributions of Stokeslets. J. Eng. Math., v. 30, pp. 35-78.

[20] S. Goldstein, private communication, 2003.

[21] R. Dillon and L. Fauci, 2000. An integrative model of internal axoneme mechanics and external fluid dynamics in ciliary beating. J. Theor. Biol., v. 207, pp. 415-430.

[22] R. Dillon, L. Fauci, C. Omoto, 2002. Mathematical Modeling of Axoneme Mechanics and Fluid Dynamics in Ciliary and Sperm Motility. To appear in Dynamics of continuous, discrete and impulsive systems.

[23] S. Lim and C. Peskin, 2003. Simulations of the whirling instability by the immersed boundary method. SIAM J. Scientific Comp., to appear.

[24] Medovikov, A.A., 1998. High order explicit methods for parabolic equations. BIT, v. 38, n. 2, pp. 372-390.

ϵ	grid size			
	$6 \times 12 \times 12$	$6 \times 24 \times 24$	$6 \times 36 \times 36$	$6 \times 48 \times 48$
0.1	19.36	19.38	19.39	19.39
0.05	18.88	19.09	19.10	19.10
0.01	16.47	18.33	18.69	18.80
Exact	18.85	18.85	18.85	18.85

Table 1: Computed diagonal entries of the resistance matrix $\mathcal{T}$ for different regularization and discretization parameters.

ϵ	grid size			
	$6 \times 12 \times 12$	$6 \times 24 \times 24$	$6 \times 36 \times 36$	$6 \times 48 \times 48$
0.1	27.09	27.16	27.16	27.16
0.05	25.53	26.08	26.10	26.11
0.01	19.62	23.89	24.80	25.09
Exact	25.133	25.133	25.133	25.133

Table 2: Computed diagonal entries of the resistance matrix $\mathcal{R}$ for different regularization and discretization parameters.

L (cm)	L/λ	ϕ (degrees)	$\mathcal{T}_{33}$	$\mathcal{P}_{33}$	$\mathcal{R}_{33}$
5.2	5	55	0.67	0.032	0.076
7.8	5	39	0.71	0.038	0.060
9.4	5	20	0.74	0.018	0.031
3.1	3	55	0.48	0.023	0.053
7.5	7	56	0.91	0.053	0.130

Table 3: Experimental measurement of resistance coefficients as reported in [14]. All coefficients were normalized by $6\pi\mu$.

L (cm)	L/λ	ϕ (degrees)	$\mathcal{T}_{33}$	$\mathcal{P}_{33}$	$\mathcal{R}_{33}$
5.2	5	55	0.6102	0.0303	0.0816
7.8	5	39	0.6823	0.0354	0.0736
9.4	5	20	0.6605	0.0141	0.0274
3.1	3	55	0.4356	0.0221	0.0496
7.5	7	56	0.7938	0.0391	0.1294

Table 4: Numerical computation of the resistance coefficients for $\epsilon = 0.01$ and a grid of 400 cross-sections and 6 points per cross-section. All coefficients were normalized by $6\pi\mu$.

grid	$\mathcal{T}_{33}$	$\mathcal{P}_{33}$	$\mathcal{R}_{33}$
6×400	0.6102	0.0303	0.0816
12×800	0.6220	0.0316	0.0850

Table 5: Numerical computations of resistance coefficients for $L = 5.2$, $L/\lambda = 5$, pitch angle 55° and two grids with different levels of refinement. All coefficients were normalized by $6\pi\mu$.

Figure captions

1. Schematic of the volume used to derive the boundary integral formulation of Stokes flow.

2. $L2$-norm of the error in the third component of velocity on the sphere as a function of the regularization parameter ϵ. The surface of the sphere was discretized using a six-patch, 24×24 fixed grid.

3. $L2$-norm of the error in the third component of velocity on the sphere as a function of grid size, for a fixed regularization parameter $\epsilon = 0.01$.

4. Log-log plot of the discretization error in the computation of the velocity field due to a translating sphere. The two dashed lines show the error at two different locations in space. The regularization parameter was fixed at $\epsilon = 0.01$. The solid line has slope two, indicating a discretization error $O(\Delta s^2)$ for small values of $\Delta s = \Delta s_1 = \Delta s_2$ (large abscissa values).

5. Numerical computation of the velocity at two different points in the fluid for various values of ϵ. The discretization was fixed with a 60×60 grid on each of the 6 patches. The top graph shows the velocity error at a point on the surface of the sphere; the bottom graph shows the velocity error at a point far from the surface.

6. Finite helices of varying pitch. The length (viewed from the side), radius of the centerline, and thickness were held fixed.

7. The number of rotations required to swim one body length as a function of the number of pitches per body length. The bar indicates the range of rotations measured by S. Goldstein for *L. illini* [20].

8. A high-voltage transmission (HVEM) image of a *Leptonema illini*, courtesy of the Resource for the Visualization of Biological Complexity that is supported by the National Center for Research Resources, NIH RR01219. The width of the photo is 2.81 μm.

9. Schematic of a spirochete motor used to drive the motion in the dynamic simulation. The arrows indicate the motor springs that contract forcing the inner ring to rotate clockwise and the outer ring to rotate counterclockwise. The motor springs periodically reattach to the next point of the outer ring to maintain the motion.

10. Elastic spirochete shown at equally-spaced time intervals during the dynamic simulation.

11. Snapshot of a portion of the elastic spirochete and corresponding flow field on a plane perpendicular to the axis of the helix.

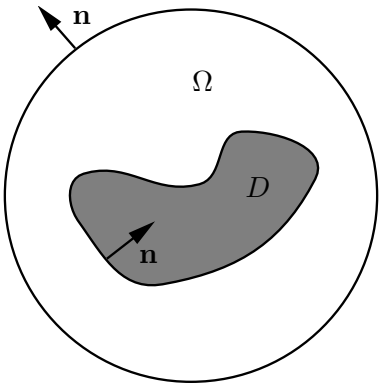

Figure 1: Cortez, Phys.Fluids

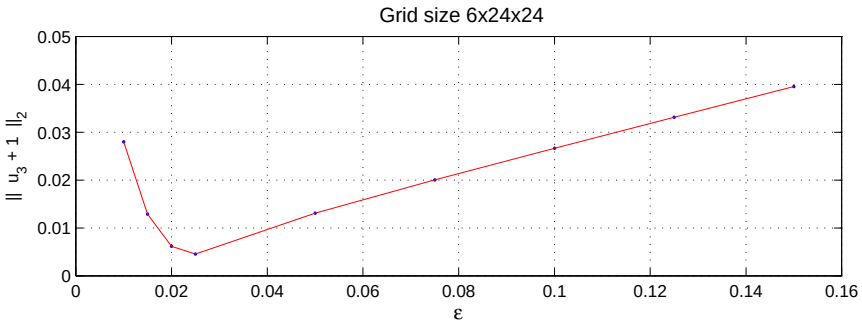

Figure 2: Cortez, Phys.Fluids

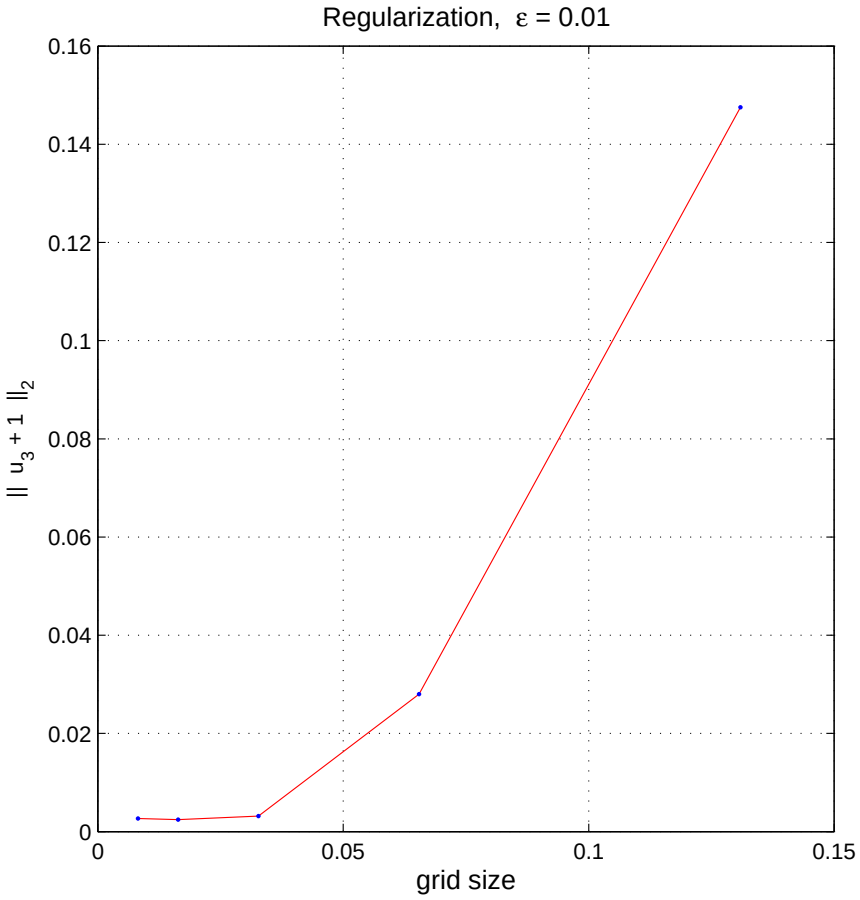

Figure 3: Cortez, Phys.Fluids

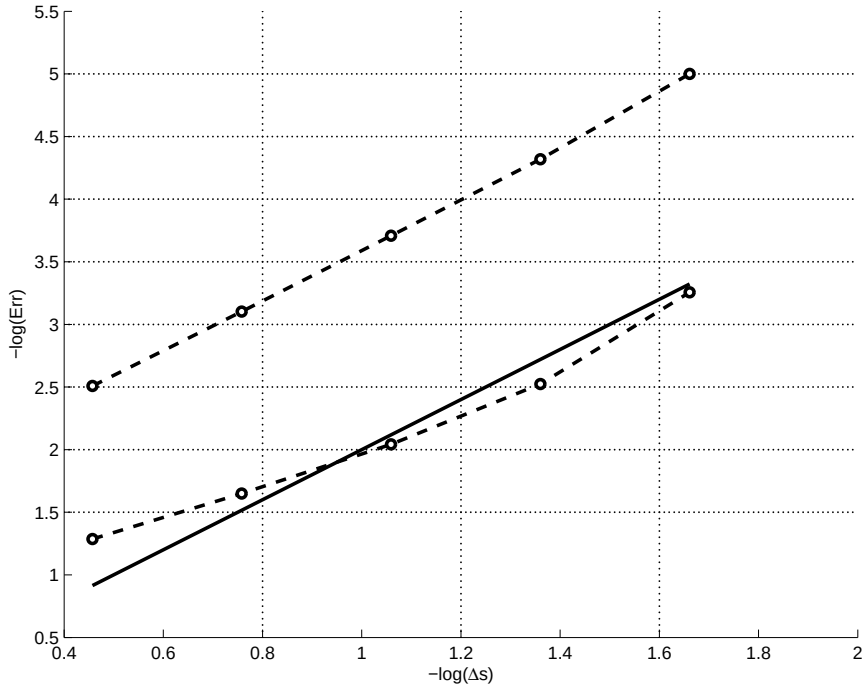

Figure 4: Cortez, Phys.Fluids

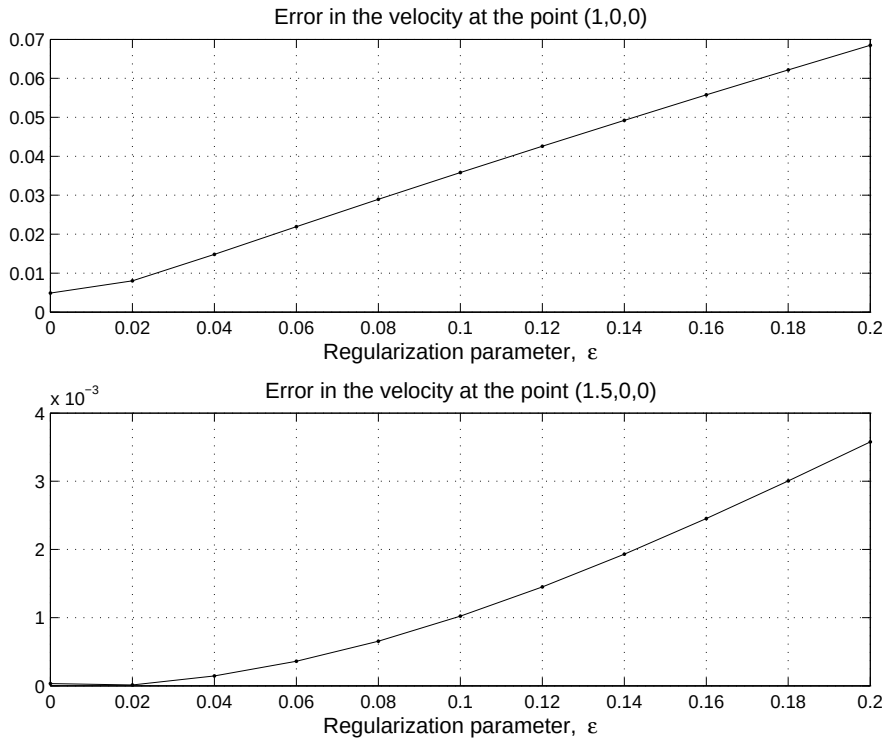

Figure 5: Cortez, Phys.Fluids

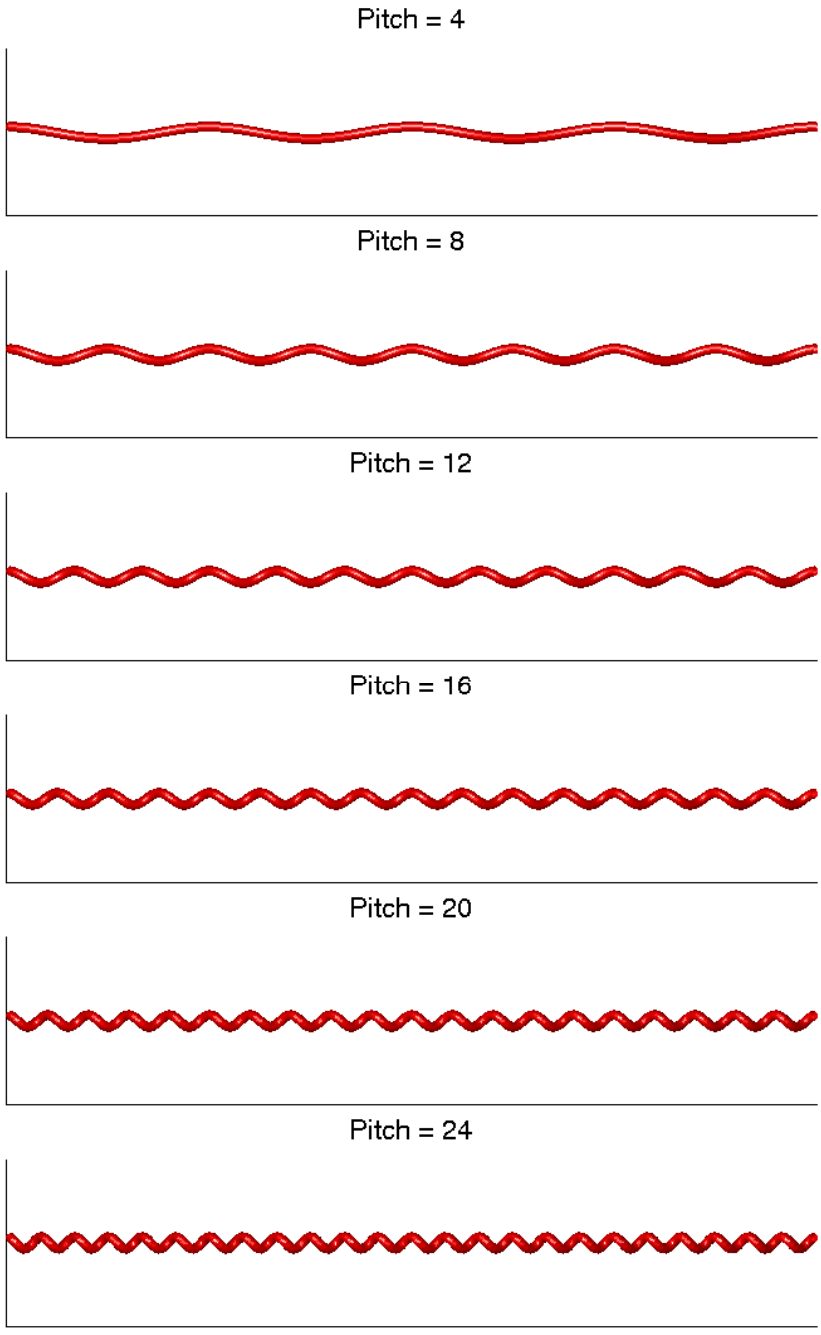

Figure 6: Cortez, Phys.Fluids

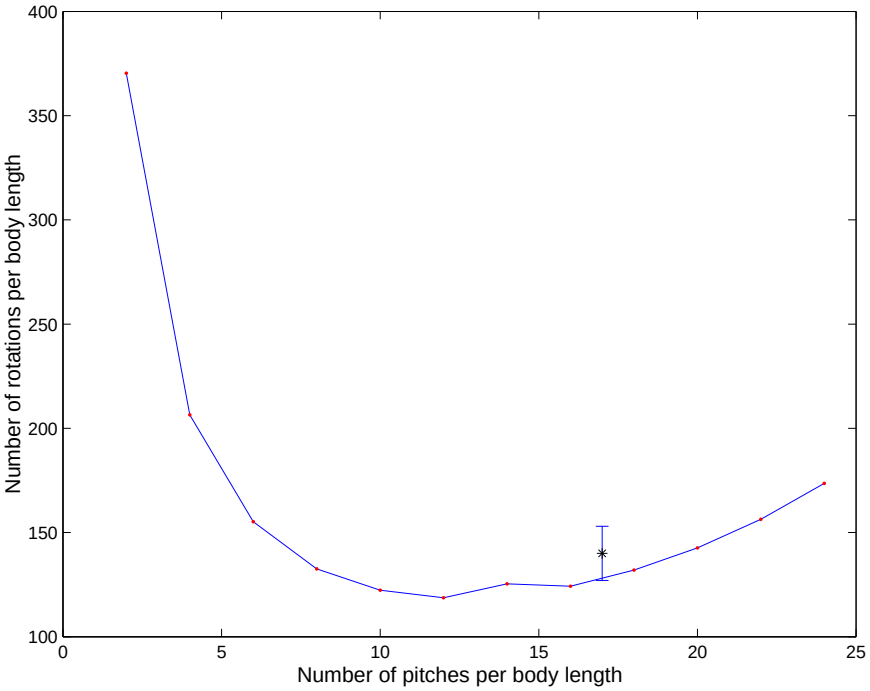

Figure 7: Cortez, Phys.Fluids

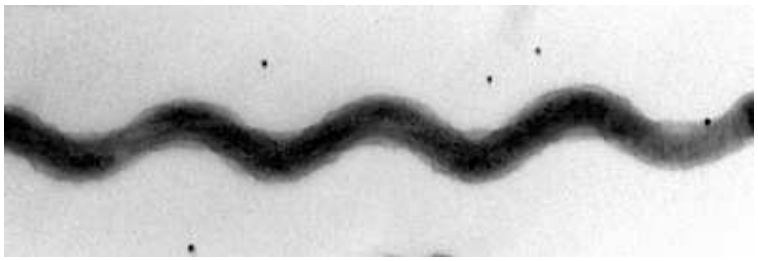

Figure 8: Cortez, Phys.Fluids

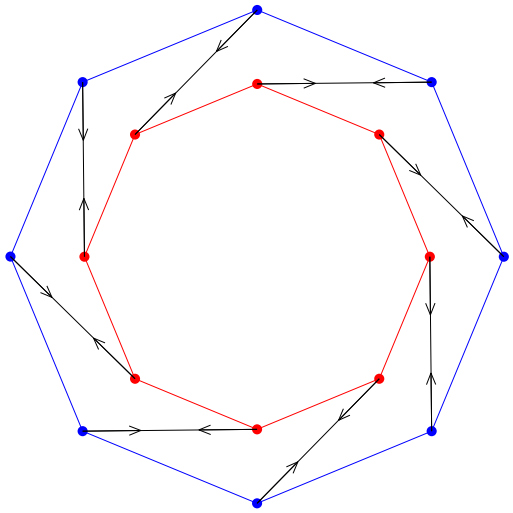

Figure 9: Cortez, Phys.Fluids

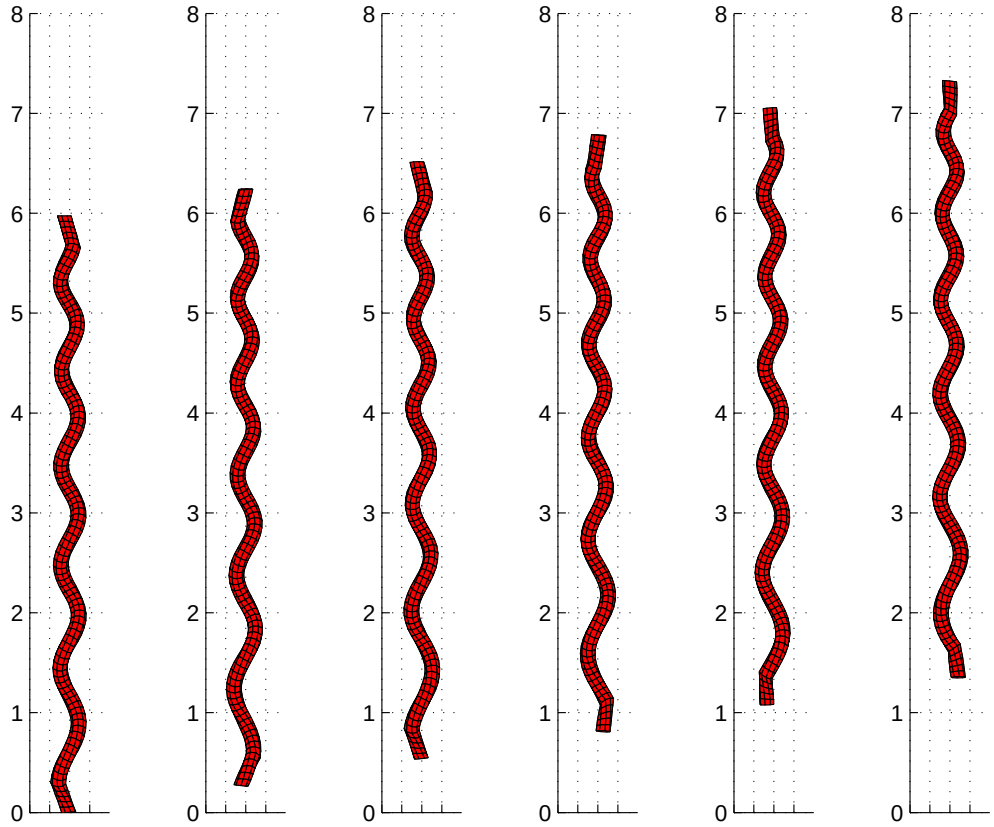

Figure 10: Cortez, Phys.Fluids

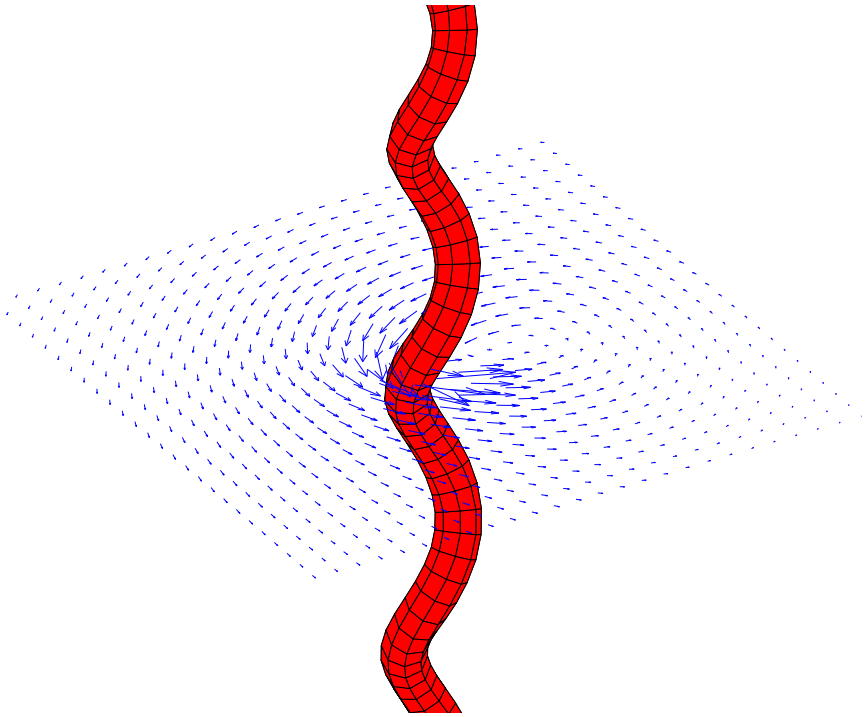

Figure 11: Cortez, Phys.Fluids